

Vat Photopolymerization 3D Printing of Hydrogels Embedding Metal–Organic Frameworks for Photodynamic Antimicrobial Therapy

*Original*

Vat Photopolymerization 3D Printing of Hydrogels Embedding Metal–Organic Frameworks for Photodynamic Antimicrobial Therapy / Wang, Yang; Frascella, Francesca; Gaglio, Cesare Gabriele; Pirri, Candido; Wei, Qufu; Roppolo, Ignazio. - In: ACS APPLIED MATERIALS & INTERFACES. - ISSN 1944-8252. - ELETTRONICO. - 16:42(2024), pp. 57778-57791. [10.1021/acsami.4c15168]

*Availability:*

This version is available at: 11583/2994924 since: 2024-12-18T09:19:22Z

*Publisher:*

American Chemical Society

*Published*

DOI:10.1021/acsami.4c15168

*Terms of use:*

This article is made available under terms and conditions as specified in the corresponding bibliographic description in the repository

*Publisher copyright*

ACS postprint/Author's Accepted Manuscript

This document is the Accepted Manuscript version of a Published Work that appeared in final form in ACS APPLIED MATERIALS & INTERFACES, copyright © American Chemical Society after peer review and technical editing by the publisher. To access the final edited and published work see <http://dx.doi.org/10.1021/acsami.4c15168>.

(Article begins on next page)



24 photoinitiator, enabling the precise printing of complex structures. In addition, these  
25 crystals impart photothermal and photodynamic capabilities to the printed object. The  
26 antibacterial assay confirms the potent photothermal/photodynamic bactericidal  
27 properties of the printed GelMA/MOF hydrogels. The hydrogel with the highest MOF  
28 content exhibited over 99.99% antibacterial efficiency against both *Gram-positive*  
29 *Staphylococcus aureus* and *Gramnegative Escherichia coli* after 30 min of light  
30 exposure ( $\sim 30 \text{ mW/cm}^2$ ,  $\lambda \geq 420 \text{ nm}$ ). Simultaneously, hemolysis and cytotoxicity  
31 evaluations validated their excellent biocompatibility. The findings presented here  
32 introduce a strategy for integrating photosensitive MOF and 3D printing to fabricate  
33 size-adjustable photothermal/photodynamic monoliths and patches, opening  
34 perspectives towards personalized treatment for wound management.

35 **Keywords:** GelMA, porphyrinic MOF, vat photopolymerization 3D printing,  
36 photothermal, photodynamic

37

38

39

40

41

42

43

44

45

## 46 **1. Introduction**

47 Over the years, wound infection has posed a major threat to human health due to  
48 the heightened vulnerability of injured skin to bacterial invasion and proliferation <sup>1</sup>.  
49 To address this issue, a substantial number of antibiotics have been developed and  
50 implemented for practical applications <sup>2</sup>. However, conventional antibiotics are  
51 becoming less effective due to the emergence of antibiotic-resistant strains resulting  
52 from their common misuse and overuse <sup>3</sup>. Therefore, alternative approaches that can  
53 effectively face bacterial infections are urgently needed. Recently, photodynamic  
54 therapy (PDT) has emerged as a promising strategy, which can inactivate pathogens  
55 by generating reactive oxygen species (ROS) through photochemical reactions.  
56 Importantly, ROS sterilize the bacteria by disrupting the cell membrane structure,  
57 thereby mitigating the concern of bacterial resistance <sup>4,5</sup>.

58 Currently, an increasing number of materials have been demonstrated to produce  
59 ROS for achieving PDT, such as carbon quantum dots (CQDs), molybdenum disulfide  
60 (MoS<sub>2</sub>), and metal-organic framework (MOF) <sup>6-8</sup>. Among them, MOF coordinated by  
61 organic linkers and metal nodes is an emerging class of photodynamic materials with  
62 ultrahigh porosity <sup>9</sup>. In particular, porphyrinic MOF possesses not only exceptional  
63 photodynamic effects but also excellent photothermal performance, making them  
64 have great potential in clinical therapeutics <sup>10</sup>. Numerous studies on porphyrinic MOF  
65 for chronic wounds, ophthalmic, and even oral treatments have been reported recently  
66 <sup>11-13</sup>. However, such nano-sized solids are not suitable for direct use in the human  
67 body due to the leakage and residual hazards, and apparently some reports on medical

68 MOF have ignored this crucial consideration. Fortunately, encapsulating and  
69 immobilizing MOF within hydrogel systems seems to be a feasible strategy. For  
70 instance, Gwon et al. employed diacrylated polyethylene glycol and 4-arm-thiolated  
71 PEG as the photocuring matrix to fabricate bioactive MOF-embedded hydrogels.  
72 These hydrogels can kill bacteria by the slow release of metal ions through the  
73 degradation of embedded MOF <sup>14</sup>. Huang et al. also reported a multifunctional  
74 composite hydrogel, which encapsulated modified curcumin-based MOF for chronic  
75 wound management <sup>15</sup>. Although these studies have highlighted the great potential of  
76 MOF-based hydrogels in wound dressings, building complex shapes and conformable  
77 patches to closely match the skin defects is also of significant importance for clinical  
78 needs <sup>16</sup>. Specifically, each patient's wound is distinct, differing in size, depth,  
79 location, and severity <sup>17</sup>. Tailoring the dressing to the specific characteristics of the  
80 wound could ensure optimal coverage and contact with the affected area, promoting  
81 effective healing <sup>18</sup>. Therefore, here we propose to employ Digital Light Processing  
82 (DLP) 3D printing technology to fabricate MOF-loaded hydrogels, aiming to satisfy  
83 the personalized antimicrobial treatment of different-shape wounds.

84 DLP is a precise and efficient additive manufacturing (AM) technique that  
85 employs a projector-based system to selectively cure photosensitive resins layer by  
86 layer, enabling to create complex three-dimensional (3D) objects <sup>19, 20</sup>. Notably,  
87 compared to other 3D printing techniques, DLP offers unique advantages such as  
88 higher printing resolution and accuracy, faster speed, and smoother surface finish <sup>21, 22</sup>.  
89 In healthcare, DLP 3D printing enables the rapid production of wound dressings

90 customized to specific shapes, which is especially crucial during emergencies when  
91 there is a sudden surge in patient demands. Furthermore, it may be compatible with  
92 the embedding of electronic components during the manufacturing process,  
93 facilitating the development of smart medical devices or dressings with real-time  
94 monitoring, diagnostic, and even therapeutic functions<sup>23,24</sup>. However, there has been  
95 limited research on DLP printed hydrogel dressings for wound therapy. Up to now,  
96 many reports have increasingly indicated that DLP is an outstanding strategy for  
97 fabricating hydrogels with complex 3D shapes employing both synthetic and natural  
98 raw materials<sup>25-30</sup>. Among different categories of bio-based hydrogel photocurable  
99 materials, gelatin methacrylate (GelMA) has been widely used in tissue engineering,  
100 wound repair, and drug release system because of its excellent biocompatibility and  
101 photopolymerizable characteristics<sup>31-33</sup>. The high optical transparency of GelMA  
102 hydrogels can provide good light transmission for the embedded photosensitizers to  
103 initiate photochemical reactions, as demonstrated by several publications<sup>34-37</sup>.

104 In this study, a porphyrinic MOF (PCN-224) composed of Zr-oxo clusters and  
105 5,10,15,20-tetrakis (4-carboxyphenyl) porphyrin (H<sub>2</sub>TCPP) ligands was chosen as the  
106 filler for the DLP 3D printing<sup>38</sup>. PCN-224 has been widely utilized as a PDT agent  
107 due to its advantages of efficient diffusion of ROS, great chemical/physical stability,  
108 and high biocompatibility<sup>38-40</sup>. To the best of our knowledge, it's the first time that  
109 porphyrinic MOF are employed as functional fillers in this advanced technology.  
110 Briefly, different concentrations of this MOF were incorporated into GelMA matrix to  
111 fabricate GelMA/MOF hydrogels using a DLP 3D printer. Taking into account the

112 light-absorption of the MOF, those can be used as smart dyes, able to improve  
113 printing precision and impart functional properties to the objects <sup>41</sup>. Consequently, the  
114 curing behavior of the GelMA/MOF formulations was measured by photorheology  
115 and printing parameters were optimized to fabricate complex shape structures. The  
116 printed GelMA/MOF hydrogels were systematically characterized by morphological  
117 observation, water retention, swelling and mechanical properties. The photothermal  
118 and photodynamic characterizations of GelMA/MOF hydrogels were also performed.  
119 In addition, the antibacterial efficiency of the GelMA/MOF hydrogels against Gram-  
120 positive *Staphylococcus aureus* (*S. aureus*) and Gram-negative *Escherichia coli* (*E.*  
121 *coli*) was evaluated under visible light ( $\sim 30$  mW/cm<sup>2</sup>,  $\lambda \geq 420$  nm). The hemolysis and  
122 cytotoxicity assays were conducted to assess the hemocompatibility and  
123 cytocompatibility, respectively. All these findings indicated that this strategy enables  
124 the customization of dressings to match the specific contours of the wound, ensuring  
125 optimal contact with the wound surface and thereby achieving effective  
126 photothermal/photodynamic therapy.

127

## 128 **2. Experimental**

### 129 **2.1 Materials**

130 The gelatine (Gel) used as precursor of gelatine methacrylate (GelMA) is Type B  
131 gelatin from bovine skin, Bloom 50-120 bought from Merck, Italy. Four types of  
132 GelMA type B (DS: 60%, 80%, 90%, 95%) were lab-synthesized following the  
133 procedures previously reported <sup>33, 42-45</sup>. ZrOCl<sub>2</sub>·8H<sub>2</sub>O (99.9%), 5,10,15,20-Tetrakis(4-

134 carboxyphenyl)porphyrin (TCPP, 97%), benzoic acid (99.5%) and 1,3-  
135 Diphenylisobenzofuran (DPBF) were purchased from Macklin Biochemical  
136 Technology, China. Water-soluble diphenyl (2,4,6-trimethylbenzoyl)phosphine oxide  
137 (TPO-SDS) and other chemicals were obtained from Merck, Italy. All chemicals were  
138 used as obtained without further purification.

## 139 **2.2 Synthesis of MOF (PCN-224) nanoparticles**

140 PCN-224 nanoparticles were synthesized according to previous method <sup>38</sup>. In  
141 brief, 1.5 g of benzoic acid and 0.15 g of  $ZrOCl_2 \cdot 8H_2O$  were dissolved in 10 mL  
142 DMF under ultrasonication, then 0.05 g of TCPP was added in the DMF with  
143 continuous ultrasonication. After that, the mixture was transferred in a Pyrex vial and  
144 heated at 120 °C for 24 h. After the reaction, the mixture was naturally cooled to room  
145 temperature and centrifuged (8000 rpm/min, 30 min) to obtain the precipitated  
146 product. Subsequently, the product was washed with DMF twice and ethanol three  
147 times to remove impurities. Finally, PCN-224 nanoparticles were collected after  
148 drying in a vacuum oven at 60 °C for 12 h.

## 149 **2.3 Formulations**

150 GelMA/MOF formulations containing different concentrations (0.125, 0.25, 0.5,  
151 1 mg/mL) of MOF nanoparticles were prepared, the notation used was GelMA/MOF<sub>x</sub>  
152 where x represents the concentration of MOF in the formulation. In detail, TPO-SDS  
153 (5% to GelMA, w/w) and GelMA were dissolved in deionized water (DI water) under  
154 ultrasonication to obtain GelMA precursor solution (30%, w/v). Then, MOF  
155 nanoparticles were ultrasonically dispersed in DI water at different concentrations

156 (0.25, 0.5, 1, 2 mg/mL). Afterward, equal volumes of the GelMA precursor solution  
157 and each MOF dispersion were mixed and vigorously stirred to obtain pre-printed  
158 GelMA/MOF formulations. The GelMA precursor solution was mixed with an equal  
159 volume of DI water to prepare pre-printed GelMA formulations, the final tested  
160 concentrations were: 10%, 12.5%, 15% and 20% w/v.

#### 161 **2.4 3D printing process**

162 The printing process of the formulations was carried out with the DLP 3D printer  
163 (Asiga UV MAX27, Asiga, AUS) to fabricate GelMA and GelMA/MOFs hydrogels.  
164 Before the printing, various shapes of models were created using Cinema 4D software  
165 and converted in STL format.

166 Preliminary tests were carried out to assess light intensity and layer thickness.  
167 The formulations were dropped on a vat and exposed for different times under LED  
168 light with 40 mW/cm<sup>2</sup> intensity. Then, the formulations were exposed for a fixed time  
169 to different light intensities to investigate the relationship between light intensity and  
170 layer thickness.

171 The light intensity and the exposure time of each formulation was selected based  
172 on these results; briefly, the slice thickness was settled as 0.2 mm. After the printing  
173 process, each sample was carefully washed by 50 °C DI water to remove uncured  
174 formulations and then post-cured for 2 min in a UV chamber. For sterilization, the  
175 post-cured hydrogels were immersed in 70% ethanol for 1 h and kept in sterile  
176 phosphate buffered solution (PBS) at 4 °C.

#### 177 **2.5 Characterization**

178 The morphology of synthesized MOF was observed by a transmission electron  
179 microscope (TEM, JEM-2100, Japan), and the average diameters and size  
180 distributions of MOF were measured by using Nano Measurer (China). The crystal  
181 structure of MOF was characterized by X-ray diffractometer (XRD, D2 PHASER,  
182 Germany), and the scanning angle was ranged from 2° to 40° with a step size of  
183 2°/min. NEXUS 470 spectrometer (USA) was employed to record the Fourier  
184 transform infrared spectroscopy (FTIR). Photorheological measurements were  
185 performed using a rheometer (Physica MCR 302, Austria) with a broad band UV-light  
186 source (Hamamatsu LC8 lamp, Japan) at light intensity of 45 mW/cm<sup>2</sup>. The  
187 morphologies of printed GelMA and GelMA/MOF hydrogels were characterized by a  
188 field emission scanning electron microscope (FESEM, Regulus8100, Japan). The UV-  
189 vis spectra were measured by a BioTek Synergy HTX Multimode Reader (USA). The  
190 mechanical property of printed hydrogels was tested by using dynamic mechanical  
191 analysis (DMA, METTLER TOLEDO DMA 1, Switzerland). All cylindrical  
192 hydrogels ( $\Phi = 10$  mm,  $H = 6$  mm) were carried out in compression mode  
193 (Displacement = 0.05 mm, Frequency = 10 Hz) at 25 °C and 37 °C. The ASIGA 3D-  
194 printer (Max-UV27, Alexandria, AUS) was employed for DLP 3D printing process,  
195 the printer employs a light source of 385 nm and has a nominal X-Y resolution of  $27 \times$   
196  $27 \mu\text{m}^2$ . A 3D optical scanner (E3, 3Shape, Denmark) was utilized to evaluate print  
197 resolution.

## 198 **2.6 Swelling and water retention tests**

199 The swelling behavior and water retention of the printed hydrogels were

200 measured according to pervious methods with slight modifications <sup>46, 47</sup>. For the  
201 swelling behaviors, the printed cube sample ( $4 \times 4 \times 4 \text{ mm}^3$ ) was freeze-dried to  
202 obtain a dry weight ( $W_0$ ). Then, the lyophilized samples were transferred to PBS  
203 solution and incubated in  $37 \text{ }^\circ\text{C}$  water for 48 h. At every interval, the sample was  
204 carefully wiped with filter paper and weight as ( $W_t$ ). The swelling rate was calculated  
205 according to Eq. (1):

$$206 \quad \textit{Swelling ratio} (\%) = \frac{W_t - W_0}{W_0} \times 100 \quad (1)$$

207 Regarding the water retention test, a cube sample ( $4 \times 4 \times 4 \text{ mm}^3$ ) was immersed  
208 in PBS for 24 h, then the sample was carefully wiped with filter paper to remove the  
209 excess moisture and weight as ( $W'_0$ ). The sample was placed at room temperature  
210 (humidity: around 40%) and weighed it at different intervals ( $W'_t$ ). The water  
211 retention was calculated according to Eq. (2):

$$212 \quad \textit{Water retention} (\%) = \frac{W'_t}{W'_0} \times 100 \quad (2)$$

## 213 **2.7 Degradation test**

214 The degradation test was conducted according to a reported method <sup>48</sup>. In brief,  
215 the freeze-dried hydrogels were added into pre-weighted plastic bottles ( $W_b$ ) and  
216 subsequently re-weighted ( $W_0$ ). Then, 4 mL of PBS were added into each bottle and  
217 the specimens were incubated at  $37 \text{ }^\circ\text{C}$ . At intervals of 1, 4, 8, 15, and 30 days, the  
218 liquid in the corresponding bottles was removed and the bottles were dried in a  
219 vacuum oven. The dried bottles were weighed ( $W_t$ ) and the degradation percentage ( $D$ )  
220 was calculated using the Eq. (3):

221 
$$D (\%) = \frac{W_t - W_b}{W_0 - W_b} \times 100 \quad (3)$$

222 **2.8 Singlet oxygen (<sup>1</sup>O<sub>2</sub>) generation detected by DPBF**

223 DPBF was used as a specific probe to detect the <sup>1</sup>O<sub>2</sub> generation. Briefly, 4 mL of  
224 50% ethanol containing DPBF (30 mg/L) was added to a plastic tube, then a printed  
225 cylindrical sample ( $\Phi = 10$  mm,  $H = 1$  mm) was added in the bottom of this tube and  
226 keep in the dark for 1 h. After that, this tube was exposed to an illumination (520 nm  
227 laser) for 5 min. 200  $\mu$ L of the solution in this tube was pipetted in a 96 well-plate and  
228 the UV-vis spectrum was recorded with a microplate reader every 1 min; in addition,  
229 the solution after each measurement was pipetted back into the tube for the next  
230 exposure.

231 **2.9 Antibacterial efficiency and SEM images of bacterial morphology**

232 The biocidal efficacy of printed GelMA and GelMA/MOF hydrogels against *S.*  
233 *aureus* (ATCC 6538) and *E. coli* (ATCC 43895) were evaluated by a modified  
234 AATCC 100-2004 Test <sup>49, 50</sup>. In detail, the sterile samples ( $\Phi = 10$  mm,  $H = 1$  mm)  
235 were respectively placed on the bottom of a sterile 24-well plate, and 10  $\mu$ L of  
236 bacterial suspension ( $10^6$  colony-forming units/mL) was inoculated on each sample.  
237 Then, a Xenon lamp ( $\sim 30$  mW/cm<sup>2</sup>,  $\lambda \geq 420$  nm) illuminated each sample for 30  
238 minutes at a vertical height. Meanwhile, the same samples were tested in another 24-  
239 well plate under darkness. Afterwards, 1 mL PBS was added to each well and  
240 vortexed for 30 s to suspend bacteria, then the bacterial suspension was diluted  
241 serially 3 times (10, 100, 1000-fold) and 50  $\mu$ L of the dilution was evenly dropped on  
242 agar plates. After incubation at 37 °C for 16-24 h, the bacterial colonies on agar plates

243 were counted. All the biocidal experiments were carried out in triplicate.

## 244 **2.10 Hemolysis and Cytotoxicity assays**

245 The hemolysis assay was conducted according to a previous method<sup>51</sup>. In detail,  
246 5 mL of anticoagulant whole blood was added to 10 mL of PBS solution and  
247 centrifuged at 1500 rpm for 10 min to collect the underlying red blood cells (RBCs).  
248 Then the obtained RBCs were injected in PBS to prepare 5% (v/v) RBCs/PBS  
249 dilution. Afterwards, 0.5 mL of RBCs/PBS dilution was mixed with 1 mL of DI water  
250 or PBS and incubated for 3 h to establish the positive or negative group. Meanwhile,  
251 0.5 mL of RBCs/PBS dilution was added to 1 mL of PBS containing 10 mg of freeze-  
252 dried GelMA or GelMA/MOF hydrogels, and co-incubated for 3 h to establish the  
253 experiment groups. These mixtures were centrifuged at 2000 rpm for 10 min after the  
254 incubation, and the absorbance of each supernatant was recorded by using a UV-vis  
255 spectrophotometer. The hemolysis ratio was calculated by Eq. (4):

$$256 \quad \text{Hemolysis ratio (\%)} = \frac{A_{\text{hydrogel}} - A_{\text{negative}}}{A_{\text{positive}} - A_{\text{negative}}} \times 100 \quad (4)$$

257 where  $A_{\text{positive}}$ ,  $A_{\text{negative}}$ , and  $A_{\text{hydrogel}}$  represent the absorbance of positive, negative,  
258 and freeze-dried hydrogel groups at 540 nm, respectively.

259 The *in vitro* cytotoxicity of printed GelMA and GelMA/MOF hydrogels was  
260 performed by CCK-8 assay method using mouse fibroblast cells (L929)<sup>52</sup>. Briefly, the  
261 L929 cells were revived in Dulbecco's Modified Eagle Medium (DMEM) under a 5%  
262 CO<sub>2</sub> atmosphere at 37°C, subsequently seeded in a 96-well plate and cultured for 24 h.  
263 Meanwhile, 10 mg of sterile hydrogel samples were incubated in DMEM at 37°C for  
264 24 h to obtain the sample extracts. Afterward, the culture medium in the 96-well plate

265 was aspirated and replaced with an equivalent volume of sample extracts. In addition,  
266 the 0.1% Triton X-100 was used as the positive control and DMEM as the negative  
267 control. The plate was then incubated for an additional 48 hours. The absorbance of  
268 the cell culture medium was measured at 450 nm after the addition of CCK-8 reagent.  
269 The cell viability of hydrogel samples was calculated by Eq. (5):

$$270 \quad \text{Cell viability (\%)} = \frac{OD_{\text{sample}} - OD_{\text{positive}}}{OD_{\text{negative}} - OD_{\text{positive}}} \times 100 \quad (5)$$

271 where  $OD_{\text{positive}}$ ,  $OD_{\text{negative}}$ , and  $OD_{\text{sample}}$  represent the absorbance of positive  
272 control, negative control, and hydrogel sample groups, respectively.

### 273 **2.11 Statistical analysis**

274 The statistical analysis employed ANOVA and Student's t-test. All experimental  
275 data were presented as mean  $\pm$  standard deviation, with statistical significance  
276 determined at  $P < 0.05$ . The standard deviations in all figures were represented by  
277 error bars.

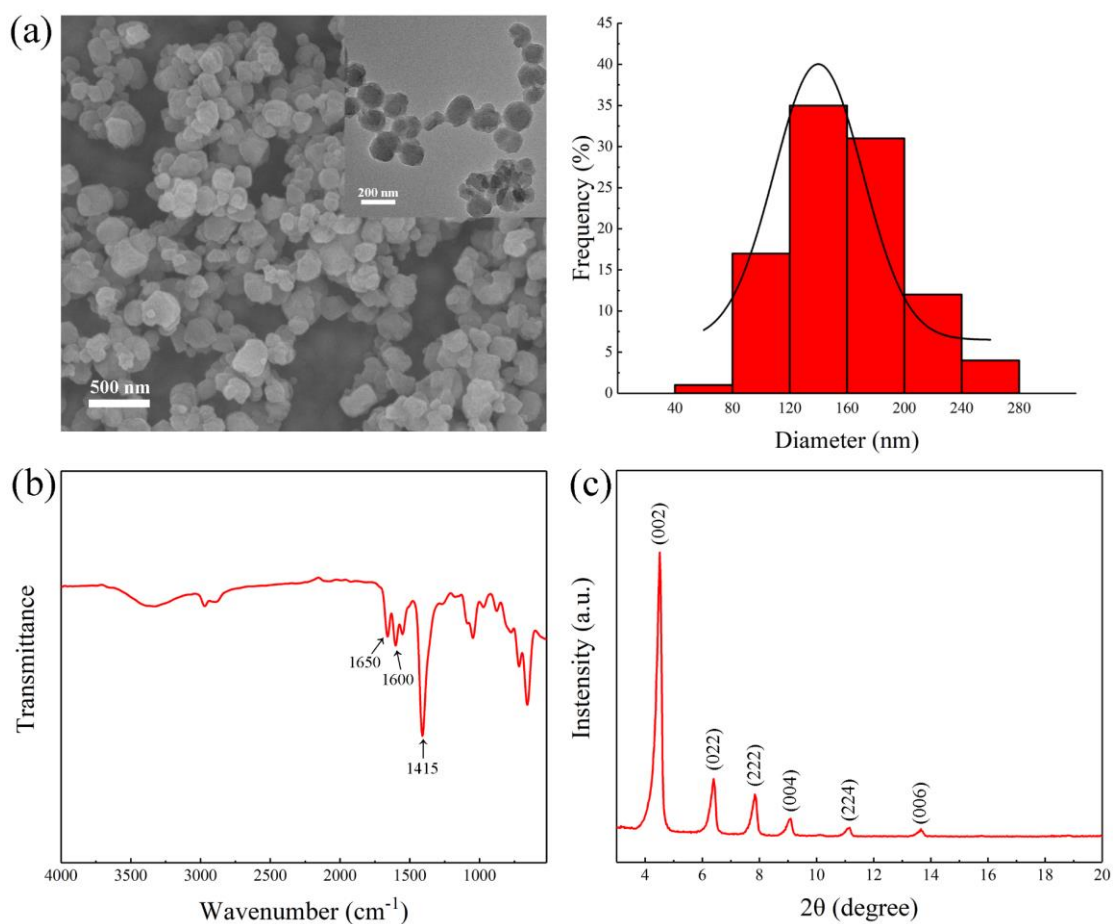
278

## 279 **3. Results and discussions**

### 280 **3.1. Synthesis and characterization of MOF**

281 The FESEM and TEM images in Fig. 1a illustrate the synthesis of MOF particles,  
282 which exhibit a predominantly spherical crystal morphology with an average diameter  
283 of approximately 158 nm and a size range spanning from 77 to 257 nm. The chemical  
284 and physical structures of the synthesized MOF were characterized by FTIR and XRD,  
285 respectively. As shown in FTIR spectrum (Fig. 1b), the peak around  $1650 \text{ cm}^{-1}$ ,  $1600$   
286  $\text{cm}^{-1}$ , and  $1415 \text{ cm}^{-1}$  were ascribed to C=O stretching vibration, C=C stretching

287 vibration and C-N bending vibration, respectively <sup>3</sup>. The XRD pattern exhibited  
288 several strong peaks around 4.6°, 6.4°, 7.9°, 9.1°, 11.2° and 13.7°, corresponding to  
289 the (002), (022), (222), (004), (224), and (006) crystal facets of PCN-224, respectively  
290 <sup>53</sup>. The results of FTIR and XRD characterizations are consistent with previous  
291 reports, confirming the successful synthesis of MOF (PCN-224) nanoparticles <sup>50</sup>.



292

293 Fig. 1. (a) Morphology images and diameter distribution of the synthesized MOF. (b)

294

FTIR spectrum of MOF. (c) XRD patterns of MOF.

295

### 296 3.2. Formulation design

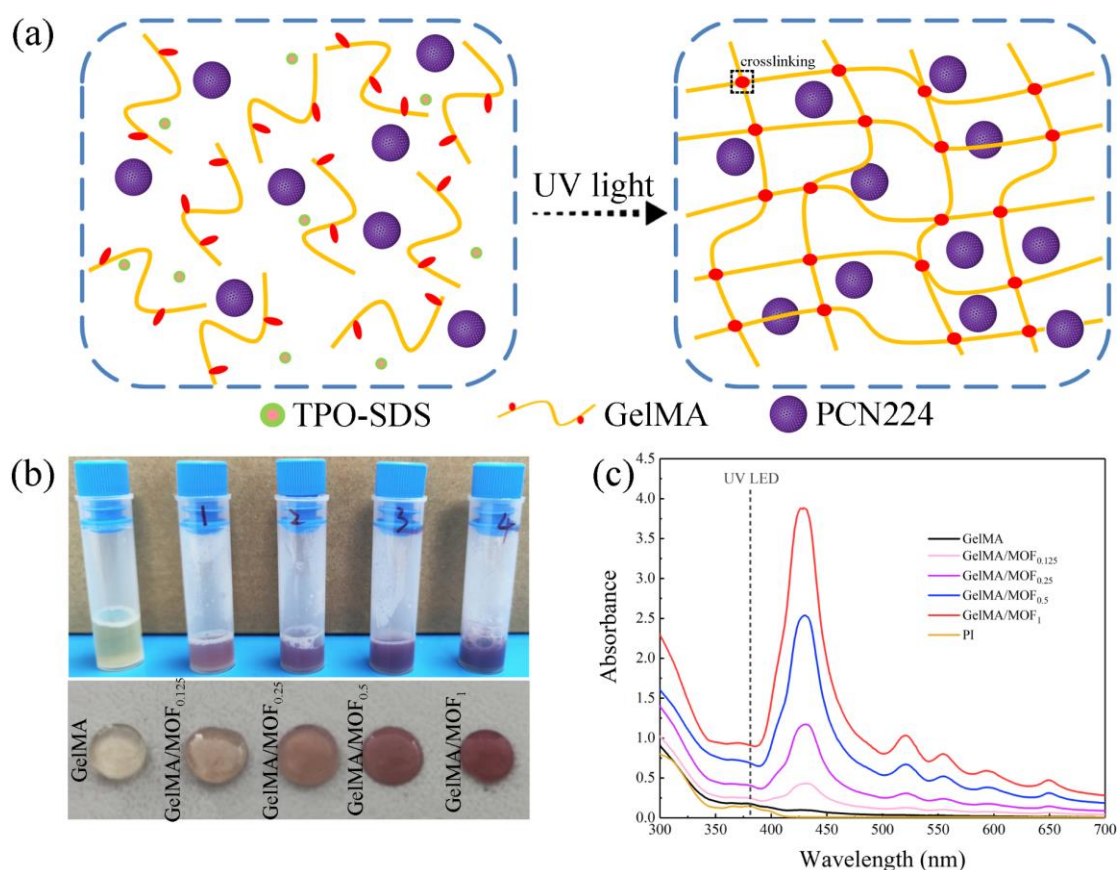
297

In preliminary experiments, GelMAs with different degrees of methacrylation  
298 (60%, 80%, 90%, and 95%) were used to print cubic hydrogels. Each type of GelMA

299 was printed at different concentrations of 10%, 12.5%, 15%, and 20% w/v in PBS or  
300 DI water. As shown in Fig. S1 in Supporting Information file, the GelMA  
301 formulations at low concentrations (10% and 12.5%) exhibited problematic cubes'  
302 printing, while the high concentration (20%) adversely affected the transparency. In  
303 contrast, the GelMA hydrogels with a concentration of 15% displayed better  
304 printability and transparency. Especially GelMA with a methacrylate substitution  
305 degree of 90% (GelMA<sub>90</sub>) showed the best printing result. Therefore, GelMA<sub>90</sub> at a  
306 concentration of 15% was used as the polymer matrix for the preparation of  
307 GelMA/MOF formulations.

308 The schematic illustration of GelMA/MOF hydrogel formation mechanism is  
309 depicted in Fig. 2a. After exposure to UV light, the GelMA molecules are covalently  
310 crosslinked, forming a dense and stable gel network that encapsulates MOF  
311 nanoparticles. Fig. 2b exhibits the GelMA and GelMA/MOF formulations and the  
312 corresponding hydrogels. Obviously, GelMA formulation can form a highly  
313 transparent hydrogel after photopolymerization. After adding MOF, the color of  
314 various GelMA/MOF formulations and their corresponding hydrogels turned to  
315 darker with increasing MOF concentration. The UV-vis absorbance spectra of GelMA,  
316 GelMA/MOF formulations and photoinitiator (PI) solution (0.75%, w/v) were  
317 measured. As exhibited in Fig. 2b, the introduction of MOF leads to enhanced light  
318 absorption at 385 nm, meaning a competition for light absorption between MOF and  
319 PI, which would affect the photopolymerization of GelMA during the printing process.  
320 This competition could be useful for DLP to improve the printing precision and to

321 prevent undesired curing out of the exposed areas <sup>41</sup>. To testify this, the GelMA and  
 322 various GelMA/MOF formulations were printed using two STL models: one featuring  
 323 a cube with vertical cylindrical holes and the other with horizontal cylindrical holes.  
 324 As depicted in Fig. S2a, the GelMA ink encounters challenges in forming the desired  
 325 hole inside the cube due to excessive photopolymerization. In contrast, Fig. S2b  
 326 demonstrates that the internal hole structure appears to be more easily printed after  
 327 incorporating the MOF. This phenomenon indicates that adding a moderate amount of  
 328 MOF can enhance printing accuracy, enabling the creation of 3D objects with more  
 329 complex structures.



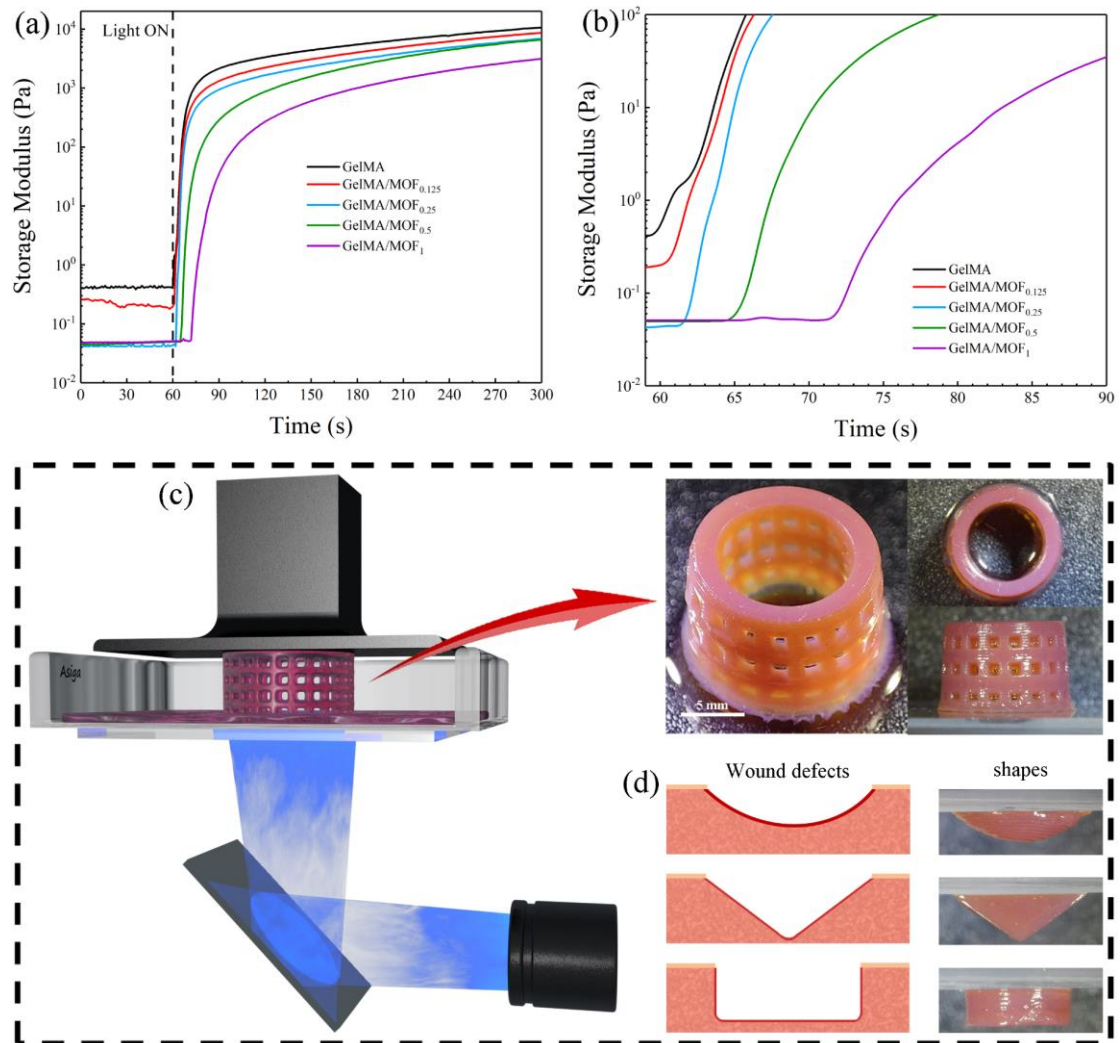
330  
 331 Fig. 2. (a) Schematic illustration of the cross-linked network of GelMA/MOF  
 332 hydrogel. (b) Photographs of various formulations and corresponding hydrogels. (c)  
 333 UV-vis absorbance spectra of GelMA formulation, GelMA/MOF formulations and PI

334 solution (0.75%, w/v).

335 Considering the effect of different MOF concentrations on photopolymerization,  
336 additional investigations were further conducted to determine the DLP printing  
337 parameters, specifically photorheology and curing behavior tests. As shown in Fig. 3a,  
338 all the formulations show rapid increase of  $G'$  modulus, indicating that gels are  
339 formed in relatively short periods upon UV irradiation. This is a first indication of  
340 their suitability for DLP 3D printing, in principle. However, the presence of MOF  
341 induced variations in the photopolymerization kinetics of GelMA matrix. The start of  
342 curing reaction of the GelMA/MOF formulations was gradually delayed as the MOF  
343 concentrations increased (Fig. 3b), witnessed by an increased latency time (up to 13 s  
344 for GelMA/MOF<sub>1</sub>). Meanwhile, also, the final storage modulus of the cured hydrogels  
345 decreases, indicating less cross-linked networks. These phenomena can be ascribed to  
346 the competition of UV light between MOF and PI, which decreases the rate of  
347 photoinitiation and thus the final conversion of acrylic double bonds<sup>41</sup>. To further  
348 determine the parameters for printing process, the curing behavior of GelMA and  
349 GelMA/MOF formulations were tested. As shown in Fig. S3a, these curves describe  
350 the relationships between the light intensity and curing thickness of the formulations.  
351 In addition, the relationships between the exposure time and the curing thickness are  
352 also tested (Fig. S3b). As expected, the curing thickness and the exposure time are  
353 linearly correlated at a constant light intensity<sup>54</sup>. These results are important for  
354 establishing optimal parameters in practical printing.

355 After optimizing the printing parameters, the fabrication of the GelMA/MOF

356 hydrogels was conducted. Fig. 3c illustrates the fabrication process using the DLP  
357 printer. This equipment is based on the localized irradiation of pixels, following a  
358 digital model file, which enables the fabrication of a single layer of one object. Then,  
359 the solidified layer was moved upward, allowing the bottom of the vat to be covered  
360 with a new layer of uncured resins, and consequently allowing to perform this process  
361 over and over, until obtaining the desired 3D object <sup>55</sup>. In this case, once the curing  
362 behavior was determined, the GelMA/MOF hydrogels with complex 3D structures  
363 could be printed, obtaining objects with well-defined edges and holes, also in z  
364 direction. It must be noted that such complexity is not trivial for formulations which  
365 contain more than 80% of water, and the definition here obtained is in good  
366 agreement with the results obtained in vat photopolymerization for formulations with  
367 similar GelMA content <sup>56</sup>. Fig. S4 demonstrates the high model fidelity achieved by  
368 DLP 3D printing, with errors of the object measured basically within 0.1 mm. In  
369 addition, Fig. 3d exhibits the various shapes of GelMA/MOF hydrogels printed  
370 according to different wound defects, implying the potential to flexibly manufacture  
371 hydrogels matching the wound defect using DLP technology, thereby enabling  
372 personalized wound management.



373

374 Fig. 3. (a) Photorheological curves of GelMA and GelMA/MOF formulations. (b)

375 Photopolymerization kinetics of GelMA and GelMA/MOF formulations within 30 s

376 of UV irradiation. (c) Schematic illustration of the printing process and the

377 corresponding product. (d) Various shapes of wound defect models and their

378 corresponding printed GelMA/MOF hydrogels.

379

### 380 3.3. Characterization of 3D-printed GelMA/MOF hydrogels

381 The micro-structure of the 3D-printed hydrogels were observed by FESEM after

382 freeze-drying. Fig. 4a and b show that the morphology of lyophilized 3D-printed

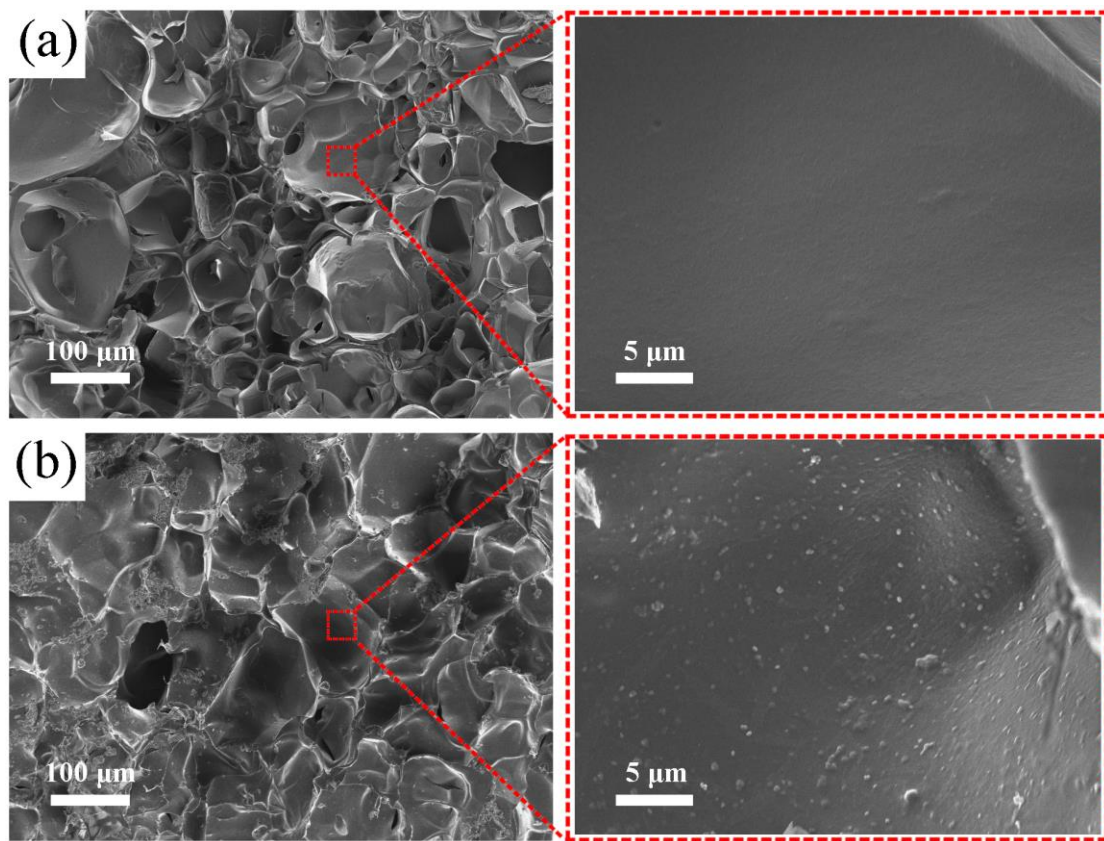
383 GelMA and GelMA/MOF<sub>1</sub> hydrogels contain highly anisotropic networks and typical  
384 microporous structure, consistent with a cross-linked internal structure and suggesting  
385 large liquid absorption capacity. In comparison of the magnified images of Fig. 4a  
386 and b, the GelMA shows a relatively smooth surface, while GelMA/MOF<sub>1</sub> shows a  
387 rougher surface, which can be attributed to the presence of the insoluble granular  
388 MOF in GelMA matrix. The effect of the higher content of MOF are here showed, but  
389 similarly the GelMA/MOF<sub>0.125</sub>, GelMA/MOF<sub>0.25</sub>, and GelMA/MOF<sub>0.5</sub> specimens  
390 display the cross-linked and microporous structure, as reported in Fig. S5 in  
391 Supporting Information file. Therefore, it can be inferred that the MOF (as the filler)  
392 plays a role during curing, but once optimized printing parameters exerts little  
393 influence on the micro-structure of photopolymerized GelMA matrix, owing to the  
394 precise control offered by DLP technology for photopolymerization.

395 The mechanical properties of the 3D-printed GelMA/MOF hydrogels were  
396 assessed by DMA at 25 °C and 37 °C. As shown in Fig. 5a and b, the storage modulus  
397 of GelMA-based hydrogel initially increases and then decreases with the increasing  
398 concentration of MOF in the system. The probable cause of this phenomenon lies in  
399 that at lower concentrations of MOF ( $c \leq 0.25$  mg/mL), the carboxyl groups within  
400 GelMA chains can coordinate with Zr<sub>6</sub> metal clusters present in MOF to form a more  
401 densely packed hydrogel structure<sup>57, 58</sup>. However, as the concentration of MOF  
402 continues to increase, their presence affects the photopolymerization of the GelMA  
403 matrix because of the optical competition, leading to a decrease in the crosslinking  
404 density of the hydrogel, in good agreement with photorheology tests. In addition,

405 from Fig. 5a and b, as expected the increase in temperature enhances the chains  
406 mobility, subsequently leading to a lower storage moduli <sup>59</sup>.

407 The swelling behavior and water retention of the printed hydrogels were also  
408 investigated. The result of swelling ratios (Fig. 5c) indicates that all freeze-dried  
409 hydrogels absorbed water rapidly, within 8 h, and then remained stable (measurement  
410 up to 48 h), without being destroyed. Interestingly, the swelling ratio was slightly  
411 reduced after adding a lower content of MOF ( $c \leq 0.25$  mg/mL). This decrease could  
412 be related to the higher crosslinking density of the nanofillers, which consequently  
413 limits network expansion during absorption <sup>30</sup>. On the other hand, when the MOF  
414 content is higher ( $c \geq 0.5$  mg/mL), the swelling ratio increased, potentially attributed  
415 to the looser network previously mentioned. To carefully tailor the final property of  
416 the hydrogel, several factors must be considered. On the one hand, the presence of the  
417 embedded nanofillers may hinder the movements of macromolecular chains  
418 decreasing the free volume between the GelMA chains, and thus reducing swelling.  
419 On the other hand, the effect of light absorption and printing parameters may result in  
420 decrease of crosslinking density, modifying the swelling behavior of the composite  
421 hydrogels <sup>30</sup>. Thus, according to desired applications, a proper trade-off must be  
422 conducted regarding the printability, mechanical properties, and swellability of the  
423 hydrogels. Fig. 5d exhibits the water retention capacity of printed hydrogels. All  
424 hydrogels exhibited a similar pattern, losing moisture and reaching equilibrium within  
425 8 h. In general, this is a drawback since hydrogels lose their flexibility drying. In view  
426 of extending the applicability of hydrogels, in our next project, we aim at improving

427 the water retention performance of printed hydrogels. The degradation behavior of  
428 printed hydrogels was also tested. As shown in Fig. S6, all hydrogels display good  
429 degradability within 30 days. It is also evident that hydrogels with higher crosslinking  
430 density (GelMA, GelMA/MOF<sub>0.125</sub>, and GelMA/MOF<sub>0.25</sub>) exhibited lower  
431 degradability, whereas those with lower crosslinking density (GelMA/MOF<sub>0.5</sub> and  
432 GelMA/MOF<sub>1</sub>) degraded more rapidly.



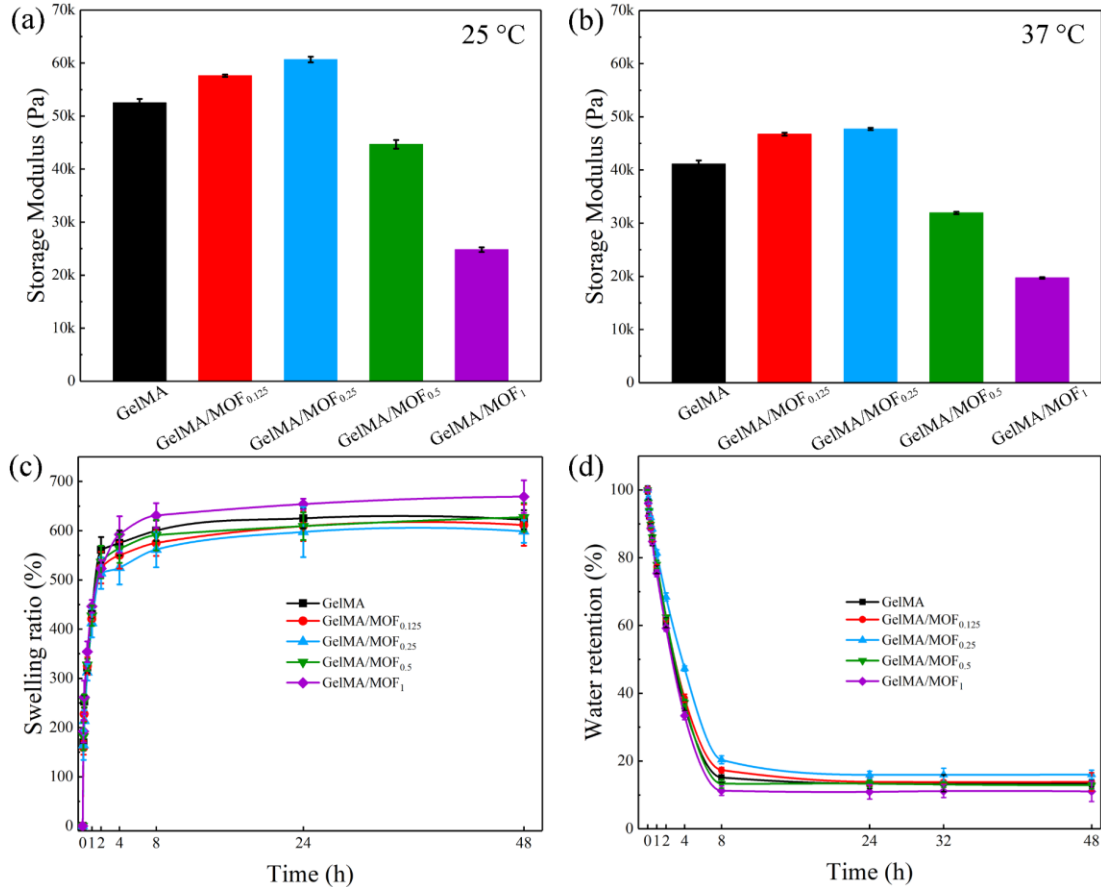
433

434 Fig. 4. Morphological structures of 3D-printed GelMA (a) and GelMA/MOF<sub>1</sub>

435

hydrogels (b).

436



437

438 Fig. 5. (a-b) Storage modulus of 3D-printed GelMA and GelMA/MOF hydrogels at

439

25 °C and 37 °C, respectively. (c) Swelling ratio. (d) Water retention.

440

441 3.4. Photothermal and photodynamic performances of printed GelMA/MOF hydrogels

442 As a subclass of MOF materials, porphyrinic PCN-224 possesses excellent

443 photothermal property and remarkable photodynamic activity<sup>38, 53, 60</sup>. Hence, the

444 photothermal and photodynamic performances of the 3D-printed GelMA/MOF

445 hydrogels were investigated. As shown in Fig. 6a to e, after exposure to visible light

446 for 180 s, the hydrogels reached a temperature of 26.7 °C for GelMA, 32.3 °C for

447 GelMA/MOF<sub>0.125</sub>, 36.4 for GelMA/MOF<sub>0.25</sub>, 40.0 °C for GelMA/MOF<sub>0.5</sub>, and 41.2 °C

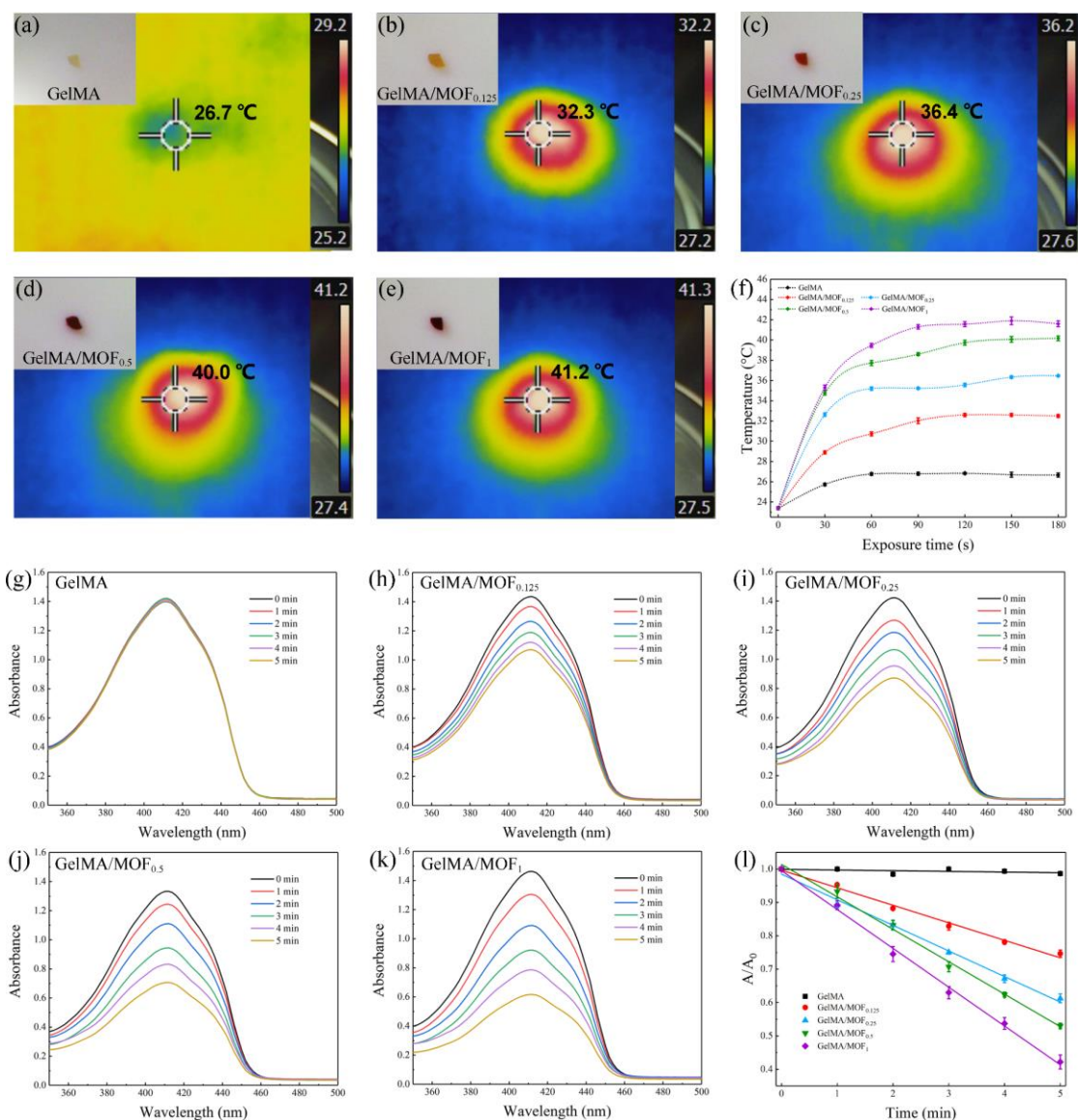
448 for GelMA/MOF<sub>1</sub>, respectively. Fig. 6f also displays the photothermal curves of these

449 printed hydrogels within 180 s. Along with the increase in the amount of MOF  
450 incorporated, the photothermal capacity gradually enhanced in the order  
451 GelMA/MOF<sub>1</sub> > GelMA/MOF<sub>0.5</sub> > GelMA/MOF<sub>0.25</sub> > GelMA/MOF<sub>0.125</sub> > GelMA.  
452 Besides, it is worth noting that all the hydrogels exhibit a similar tendency, as the  
453 exposure time to light increases, the temperature remains around its maximum value.  
454 This phenomenon may be attributed to the evaporation of water within the hydrogel  
455 system, which limits the increase in temperature.

456 PCN-224 has already been demonstrated able to produce <sup>1</sup>O<sub>2</sub> under light  
457 irradiation, which could be specifically trapped by DPBF, leading to a decrease in the  
458 absorbance at 415 nm <sup>61</sup>. Hence, DPBF was selected as the <sup>1</sup>O<sub>2</sub> detector to compare  
459 the photodynamic activity of printed GelMA/MOF hydrogels. Fig. 6g to k display the  
460 UV-vis absorption spectra of DPBF co-incubated with these hydrogels after 5 min  
461 irradiation. As predicted, the GelMA/MOF<sub>1</sub> hydrogel caused the most significant  
462 decrease of absorption at 415 nm, indicating that this material could produce the  
463 largest amount of <sup>1</sup>O<sub>2</sub>, followed by GelMA/MOF<sub>0.5</sub>, GelMA/MOF<sub>0.25</sub>,  
464 GelMA/MOF<sub>0.125</sub>, and GelMA. Similarly, the corresponding fitting curves (Fig. 6l)  
465 depicting the absorption decrease over time (at 415 nm) further suggest that the  
466 GelMA/MOF<sub>1</sub> achieved the highest efficiency in <sup>1</sup>O<sub>2</sub> yield, followed by  
467 GelMA/MOF<sub>0.5</sub>, GelMA/MOF<sub>0.25</sub>, GelMA/MOF<sub>0.125</sub>, and GelMA. Apparently, in this  
468 case, the GelMA hydrogel (without MOF) showed no reduction in DPBF absorbance  
469 under light irradiation for 5 min, confirming that the generation of <sup>1</sup>O<sub>2</sub> is attributed to  
470 the presence of the MOF. To exclude time-degradation effects, the absorption spectra

471 of DPBF co-incubated with GelMA/MOF<sub>1</sub> hydrogel in dark condition were recorded  
472 and reported in Fig. S7a. The absorbance at 415 nm remains stable after 5 min co-  
473 incubation, confirming that the degradation can be related only by the generation of  
474 <sup>1</sup>O<sub>2</sub> in MOF, activated by light irradiation. Furthermore, to investigate the possible  
475 release of the MOF crystals from the network, the printed hydrogels were sonicated in  
476 PBS at 37 °C for 1 h, and the leakage was then detected collecting UV-vis spectra. As  
477 shown in Fig. S7b, no characteristic absorption peaks of MOF were observed in any  
478 group after 1 hour of sonication. The inset of the same figure also showed that all  
479 hydrogels were not damaged during the swelling, while the supernatant remained  
480 clear and transparent. Thus, it could be inferred that the MOF crystals are effectively  
481 embedded in GelMA matrix, even after swelling. In order to test the stability of  
482 photodynamic activity, <sup>1</sup>O<sub>2</sub> detection was repeated after 30 min of exposure to visible  
483 light (~30 mW/cm<sup>2</sup>) on these GelMA/MOF hydrogels, as shown by the fitting curves  
484 of <sup>1</sup>O<sub>2</sub> yield in Fig. S8. All the GelMA/MOF hydrogels still exhibited photodynamic  
485 activity consistent with previous findings, although their <sup>1</sup>O<sub>2</sub> generation efficiency  
486 slightly decreased, while obviously GelMA didn't show any activity. This  
487 demonstrates that the embedded MOFs maintain stable and repeatable <sup>1</sup>O<sub>2</sub> generation  
488 <sup>62,63</sup>. To check whether the radical generation modifies the polymeric networks, DMA  
489 tests were repeated on these light-exposed hydrogels. As shown in Fig. S9, the storage  
490 moduli of all hydrogels at 37 °C increased compared to pre-exposure values, with  
491 more significant increases observed in hydrogels which contain higher amount of  
492 MOF. This is can be related to a water loss caused by light exposure, as the storage

493 modulus typically has a negative correlation with the water content of hydrogels <sup>64</sup>.  
 494 On the other hand, it is not possible to exclude that the radicals' generation can also  
 495 slightly modify the polymeric network, creating new cross-linking point which can be  
 496 consistent with an increase of the moduli. To better evaluate this aspect specific  
 497 ageing tests should be performed, which are beyond the scope of this manuscript and  
 498 will be better investigated in future activities.



499

500 Fig. 6. (a-e) Digital images and surface thermal under visible illumination (~30

501 mW/cm<sup>2</sup>) for 180 s. (f) Temperature rise curves. (g-k) UV-vis spectra of DPBF under

502 illumination (520 nm) in presence of GelMA and GelMA/MOF hydrogels. (l) Linear  
503 fitting of  $^1\text{O}_2$  yields.

504

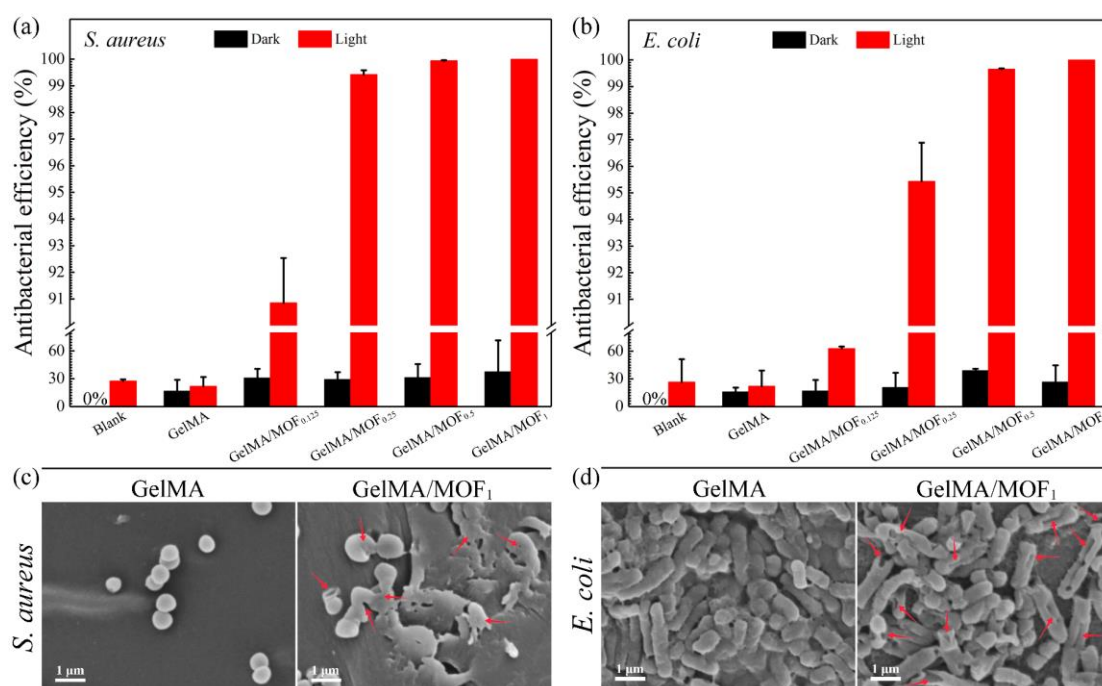
### 505 3.5. Antibacterial efficacy

506 Based on the above results, it was natural thinking that after incorporating a  
507 greater amount of MOF into the GelMA hydrogel, the photothermal and  
508 photodynamic abilities could be enhanced simultaneously. Herein, two common  
509 strains (*S. aureus* and *E. coli*), which are responsible for most wound infections, were  
510 used to evaluate the antibacterial performance of the printed GelMA/MOF hydrogels  
511 <sup>65</sup>. The bacterial suspensions without contacting printed hydrogels were set as blank  
512 groups. Fig. S10a and b displayed the surviving bacterial colonies of *S. aureus* and *E.*  
513 *coli* on LB agar plates, respectively. In comparison to the blank groups (dark and  
514 light), a minimal decrease in bacterial survival could be observed after the bacterial  
515 suspensions were exposed to the light illumination alone, indicating that the light  
516 caused almost no damage to the bacteria. In the dark groups, both *S. aureus* and *E.*  
517 *coli* grew quite well after contacting with GelMA and GelMA/MOF hydrogels for 30  
518 min. However, under light illumination, the viable colonies of both types of bacteria  
519 decreased as the MOF content increased in the GelMA/MOF hydrogels. This  
520 phenomenon demonstrates that GelMA/MOF hydrogels could effectively eliminate  
521 bacteria upon light irradiation, and the antibacterial efficiency increases together with  
522 the MOF content. The quantified antibacterial efficiencies against *S. aureus* and *E.*  
523 *coli* were displayed in Fig. 7a and b, respectively. The light alone caused a 27.29%

524 reduction against *S. aureus* and a 26.35% reduction against *E. coli*, which could be  
525 considered negligible in terms of bactericidal effect<sup>38</sup>. Additionally, all the dark  
526 groups displayed slight reduction against *S. aureus* and *E. coli*, which could be  
527 attributed to the bacterial adhesion on GelMA or GelMA/MOF hydrogels, rather than  
528 a bactericidal action. After the hydrogels were illuminated under light, GelMA/MOF<sub>1</sub>  
529 hydrogel exhibited the highest antibacterial efficiency against *S. aureus* (> 99.99%)  
530 and *E. coli* (> 99.99%), followed by GelMA/MOF<sub>0.5</sub> (*S. aureus*: 99.94%, *E. coli*:  
531 99.65%), GelMA/MOF<sub>0.25</sub> (*S. aureus*: 99.42%, *E. coli*: 95.43%), GelMA/MOF<sub>0.125</sub> (*S.*  
532 *aureus*: 90.85%, *E. coli*: 62.54%), and GelMA (*S. aureus*: 21.67%, *E. coli*: 21.90%).  
533 Here, the slight reduction observed in GelMA hydrogels against both *S. aureus* and *E.*  
534 *coli* also could be attributed to bacterial adhesion rather than sterilization. The results  
535 of the antibacterial tests are consistent with the findings of the  
536 photothermal/photodynamic analysis.

537 SEM was also employed to observe the morphologies of bacteria after treatment  
538 with GelMA/MOF hydrogels. Herein, bacteria were inoculated on GelMA and  
539 GelMA/MOF<sub>x</sub> hydrogels and illuminated for 30 min for comparison. As shown in Fig.  
540 7c, *S. aureus* exhibited typical morphologies with intact spherical shapes and smooth  
541 surfaces on GelMA hydrogel. However, on GelMA/MOF<sub>1</sub> hydrogel, the membranes  
542 of *S. aureus* were severely deformed and ruptured (red arrows). The same  
543 phenomenon could be observed in Fig. 7b, where *E. coli* maintained their typical and  
544 intact rod shapes on GelMA hydrogel, while appearing wrinkled and ruptured on  
545 GelMA/MOF<sub>1</sub> hydrogel (red arrows). Additionally, the bacteria treated with

546 GelMA/MOF<sub>0.125</sub>, GelMA/MOF<sub>0.25</sub>, and GelMA/MOF<sub>0.5</sub> hydrogels are shown in Fig.  
 547 S11. The morphological deformation of *S. aureus* and *E. coli* is also observed, with  
 548 the degree becoming more pronounced as the MOF content increases. Thus, the  
 549 bactericidal action of the GelMA/MOF hydrogels could be ascribed to a synergism of  
 550 MOF-triggered photothermal and photodynamic processes. This combined effect can  
 551 disrupt the structure of the bacterial membrane, leading to the outflow of intracellular  
 552 substances and ultimately triggering apoptosis<sup>66, 67</sup>.



553  
 554 Fig. 7. Antibacterial efficiencies of GelMA and GelMA/MOF hydrogels against *S.*  
 555 *aureus* (a) and *E. coli* (b). SEM images of *S. aureus* (c) and *E. coli* (d) contacted with  
 556 GelMA and GelMA/MOF<sub>1</sub> under visible light for 30 min irradiation.

557

### 558 3.6. Hemocompatibility and cytocompatibility

559 An ideal medical dressing should be biocompatible with both blood cells and  
 560 skin tissue cells<sup>68</sup>. Here, *in vitro* hemolysis and cytotoxicity assays were conducted to

561 evaluate the biocompatibilities of printed GelMA/MOF hydrogels. As depicted in Fig.  
562 8a, the hemolysis ratios of GelMA and GelMA/MOF hydrogels remained below the  
563 specified limit (5% hemolysis) after 3-hour co-incubation, indicating their good  
564 compatibility with blood cells <sup>69</sup>. The inset in Fig. 8a illustrates the supernatants of  
565 each group, where RBCs ruptured after incubation in DI water (positive control),  
566 leading to a bright red in the supernatant. Conversely, the RBCs co-incubated with  
567 GelMA and GelMA/MOF hydrogel exhibited supernatants that appeared nearly  
568 colorless and transparent, like the incubation in PBS (negative), indicating  
569 insignificant levels of hemolysis. Fig. 8b displays the cytocompatibility of printed  
570 GelMA and GelMA/MOF hydrogels. After a 48 h co-culture with L929 cells, the cell  
571 viability in all sample groups exceeded 80%, confirming the low cytotoxicity of these  
572 GelMA/MOF hydrogels <sup>70</sup>. The Live/Dead staining assay was also performed to  
573 assess the condition of L929 cells following the cytotoxicity test. As shown in Fig. 8c,  
574 the majority of spindle-shaped cells exhibited green fluorescence in negative control  
575 and all hydrogel groups, corresponding to the living cells. Few dead cells,  
576 characterized by red fluorescence and a globular shape, were observed in these groups,  
577 suggesting negligible cytotoxicity. The results of *in vitro* hemolysis and cytotoxicity  
578 assays demonstrate the favorable biocompatibility of printed GelMA/MOF hydrogels,  
579 positioning them as promising candidates for use in wound dressings.

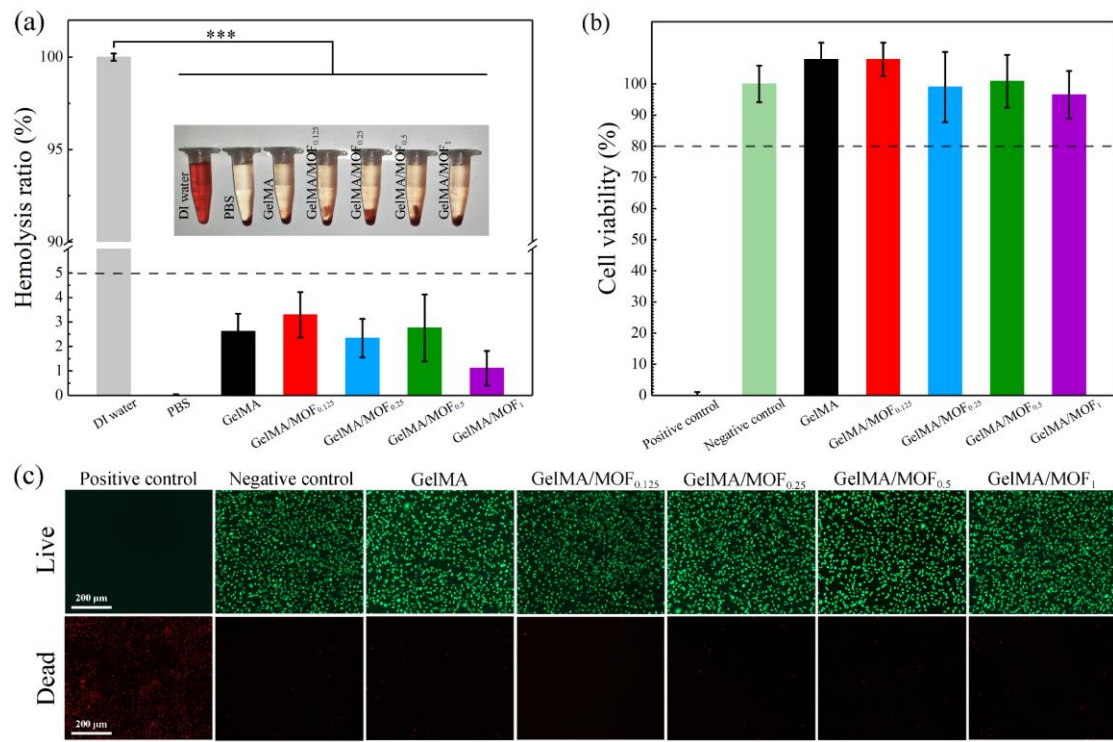


Fig. 8. (a) Hemolysis assay. (b) Cell viability of cytotoxicity assay. (c) Live/Dead staining assay. (\*\*\*) represents  $P < 0.001$ .

#### 4. Conclusions

In summary, this work reports the fabrication of printable MOF-based nanocomposite hydrogels through DLP 3D printing, utilizing photocurable GelMA resins and incorporating PCN-224 as a nanofiller. During the printing, higher UV-light intensity and longer slicing time were required due to the photo-competitive effect of the MOF, while the printing precision could be improved. This facilitates the construction of more intricate and fidelity hydrogel structures tailored to clinical wound defects. Moreover, the incorporation of MOF imparts photothermal and photodynamic properties to the printed hydrogels, with both effects amplifying as MOF concentration increases. However, a high concentration of MOF affects printing

594 and the mechanical properties of the nanocomposite hydrogels. The result of  
595 antibacterial assay revealed an enhancement in antibacterial performance with  
596 increasing MOF concentration, with GelMA/MOF<sub>1</sub> exhibiting the highest  
597 antibacterial efficiency against *S. aureus* (> 99.99%) and *E. coli* (> 99.99%) for 30  
598 min illumination, followed by GelMA/MOF<sub>0.5</sub> (*S. aureus*: 99.94%, *E. coli*: 99.65%),  
599 GelMA/MOF<sub>0.25</sub> (*S. aureus*: 99.42%, *E. coli*: 95.43%), and GelMA/MOF<sub>0.125</sub> (*S.*  
600 *aureus*: 90.85%, *E. coli*: 62.54%). Additionally, all printed GelMA/MOF hydrogels  
601 demonstrated excellent cytocompatibility and hemocompatibility. Therefore, utilizing  
602 MOF as a functional filler in the preparation of biocompatible  
603 photodynamic/photothermal hydrogels through DLP 3D printing not only mitigates  
604 the risks associated with MOF drug residue but also allows for the customization of  
605 wound dressings matching specific skin defects. In the next future, this additive  
606 approach will hold significant clinical relevance in light therapy.

607

#### 608 **Declaration of competing interest**

609 The authors declare no competing financial interest.

610

#### 611 **Supporting Information**

612 Preliminary 3D printing experiments 3D printed parts with increasing content of  
613 MOFs, 3D printing working curves, evaluation of 3D printing fidelity, additional  
614 SEM experiments on freeze-dried matrices, degradation test, leakage test, evaluation  
615 of <sup>1</sup>O<sub>2</sub> yields after ageing, DMA measurements after UV ageing, additional bacterial  
616 test and additional SEM images of bacteria are supplied as Supporting Information.

617

618 **Acknowledgments**

619 This work is supported by the funds of China Scholarship Council (No.  
620 202206790041).

621 Under the National Plan for Complementary Investments to the NRRP, project  
622 “D34H—Digital Driven Diagnostics, prognostics and therapeutics for sustainable  
623 Health care” (project code: PNC0000001), Spoke 4 funded by the Italian Ministry of  
624 University and Research.

625 **References**

- 626 (1) Dong, R.; Guo, B. Smart Wound Dressings for Wound Healing Nano Today 2021,41, 101290.  
627 (2) Chang, R.Y.K.; Nang, S.C.; Chan, H.-K.; Li J. Novel Antimicrobial Agents for Combating  
628 Antibiotic-Resistant Bacteria Adv. Drug Deliv. Rev. 2022, 187, 114378.  
629 (3) Nie, X.; Wu, S.; Mensah, A.; Wang Q.; Huang, F.; Wei, Q. FRET as a Novel Strategy to Enhance  
630 the Singlet Oxygen Generation of Porphyrinic MOF Decorated Self-Disinfecting Fabrics Chem. Eng. J.  
631 2020, 395, 125012.  
632 (4) Zhou, C.; Wang, Q.; Jiang, J.; Gao, L. Nanozybotics: Nanozyme-Based Antibacterials Against  
633 Bacterial Resistance Antibiotics 2022, 11, 390.  
634 (5) Liu, S.; Wang, B.; Yu, Y.; Liu, Y.; Zhuang, Z.; Zhao, Z.; Feng, G.; Qin, A.; Tang, B.Z.  
635 Cationization-Enhanced Type I and Type II ROS Generation for Photodynamic Treatment of Drug-  
636 Resistant Bacteria ACS Nano 2022, 16, 9130-9141.  
637 (6) Liu, C.; Chang, Q.; Fan, X.; Meng, N.; Lu, J.; Shu, Q.; Xie, Y.; Celia, C.; Wei, G.; Deng, X.  
638 Rational Construction of CQDs-Based Targeted Multifunctional Nanoplatfor for Synergistic Chemo-  
639 Photothermal Tumor Therapy J. Colloid Interf. Sci. 2024, 677, 79-90.  
640 (7) Zhao, M.; Yang, H.; Sun, Z.; Li, Y.; Hou, L.; Zhang, S.; Jin, L.; Shen, B.; Xia, B. MoS<sub>2</sub>  
641 Nanocomposites Loaded with Zinc Phthalocyanine for NIR Light-Triggered  
642 Photothermal/Photodynamic Therapy of Breast Cancer ACS Appl. Nano Mater. 2024, 7, 16372-16384.  
643 (8) Jiang, X.; Huang, Z.; Liu, Z.; Wang, S.; Qiu, Y.; Su, X.; Wang, Y.; Xu, H.; MOF-Derived Oxygen-  
644 Deficient Titania-Mediated Photodynamic/Photothermal-Enhanced Immunotherapy for Tumor  
645 Treatment ACS Appl. Mater. Interfaces 2024, 16, 34591-34606.  
646 (9) Han, X.; Boix, G.; Balcerzak, M.; Moriones, O.H.; Cano-Sarabia, M.; Cortés, P.; Bastús, N.; Puentes,  
647 V.; Llagostera, M.; Imaz, I. Antibacterial Films Based On MOF Composites That Release Iodine  
648 Passively Or Upon Triggering By Near-Infrared Light Adv. Funct. Mater. 2022, 32, 2112902.  
649 (10) Li, S.-Y.; Cheng, H.; Qiu, W.-X.; Zhang, L.; Wan, S.-S.; Zeng, J.-Y.; Zhang, X.-Z. Cancer Cell  
650 Membrane-Coated Biomimetic Platform For Tumor Targeted Photodynamic Therapy And Hypoxia-  
651 Amplified Bioreductive Therapy Biomaterials 2017, 142 149-161.  
652 (11) Chao, D.; Dong, Q.; Yu, Z.; Qi, D.; Li, M.; Xu, L.; Liu, L.; Fang, Y.; Dong, S. Specific Nanodrug  
653 for Diabetic Chronic Wounds Based on Antioxidase-Mimicking MOF-818 Nanozymes J. Am. Chem.  
654 Soc. 2022, 144, 23438-23447.  
655 (12) Chansi; Upreti, S.; Punya; Singh, J.; Ghosh, M.P.; Basu, T. Rapid Electrochemical Quantification  
656 for In Vitro Release Trait of Ophthalmic Drug Loaded within Mucoadhesive Metal Organic Framework  
657 (MOF) Chem. Select 2021, 6, 3006-3012.

- 658 (13) Li, J.; Song, S.; Meng, J.; Tan, L.; Liu, X.; Zheng, Y.; Li, Z.; Yeung, K.W.K.; Cui, Z.; Liang, Y. 2D  
659 MOF Periodontitis Photodynamic Ion Therapy *J. Am. Chem. Soc.* 2021, 143, 15427-15439.
- 660 (14) Gwon, K.; Han, I.; Lee, S.; Kim, Y.; Lee, D.N. Novel Metal–Organic Framework-Based  
661 Photocrosslinked Hydrogel System for Efficient Antibacterial Applications *ACS Appl. Mater.*  
662 *Interfaces* 2020, 12, 20234-20242.
- 663 (15) Huang, K.; Liu, W.; Wei, W.; Zhao, Y.; Zhuang, P.; Wang, X.; Wang, Y.; Hu, Y.; Dai, H.  
664 Photothermal Hydrogel Encapsulating Intelligently Bacteria-Capturing Bio-MOF for Infectious Wound  
665 Healing *ACS Nano* 2022, 16, 19491-19508.
- 666 (16) Wang, Z.; Liang, X.; Wang, G.; Wang, X.; Chen, Y. Emerging Bioprinting for Wound Healing *Adv.*  
667 *Mater.* 2023, 2304738.
- 668 (17) Farahani, M.; Shafiee, A. Wound Healing: from Passive to Smart Dressings *Adv. Healthc. Mater.*  
669 2021, 10, 2100477.
- 670 (18) Zhang, M.; Zhao, X. Alginate Hydrogel Dressings for Advanced Wound Management *Int. J. Biol.*  
671 *Macromol.* 2020, 162, 1414-1428.
- 672 (19) Salas, A.; Zanatta, M.; Sans, V.; Roppolo, I. Chemistry in Light-Induced 3D Printing *Chemtexts*  
673 2023, 9, 4.
- 674 (20) Mogli, G.; Reina, M.; Chiappone, A.; Lamberti, A.; Pirri, C.F.; Roppolo, I.; Stassi, S. Self-  
675 Powered Integrated Tactile Sensing System Based on Ultrastretchable, Self-Healing and 3D Printable  
676 Ionic Conductive Hydrogel *Adv. Funct. Mater.* 2024, 34, 2307133.
- 677 (21) Hu, Y.; Tang, H.; Xu, N.; Kang, X.; Wu, W.; Shen, C.; Lin, J.; Bao, Y.; Jiang, X.; Luo Z. Adhesive,  
678 Flexible, and Fast Degradable 3D-Printed Wound Dressings with a Simple Composition *Adv. Healthc.*  
679 *Mater.* 2024, 13, 2302063.
- 680 (22) Deng, S.; Wu, J.; Dickey, M.D.; Zhao, Q.; Xie, T. Rapid Open-Air Digital Light 3D Printing of  
681 Thermoplastic Polymer *Adv. Mater.* 2019, 31, 1903970.
- 682 (23) He, X.-C.; Chen, X.-N.; Liu, Y.-H.; Zhong, X.; Qiang, L.; Wang, H.-Q.; Wang, F.-Z.; Wang, J.-S.;  
683 Li, C.-H.; Zheng, P.-F. A Blue Light 3D Printable Hydrogel with Water Absorption, Antibacterial, and  
684 Hemostatic Properties for Skin Wound Healing *Chem. Eng. J.* 2024, 493, 152439.
- 685 (24) Tabriz, A.G.; Douroumis, D. Recent Advances in 3D Printing for Wound Healing: a Systematic  
686 Review *J. Drug Deliv. Sci. Tec.* 2022, 74, 103564.
- 687 (25) Caprioli, M.; Roppolo, I.; Chiappone, A.; Larush, L.; Pirri, C.F.; Magdassi, S. 3D-Printed Self-  
688 Healing Hydrogels via Digital Light Processing *Nat. Commun.* 2021, 12, 2462.
- 689 (26) Villata, S.; Canta, M.; Baruffaldi, D.; Pavan, A.; Chiappone, A.; Pirri, C.F.; Frascella, F.; Roppolo,  
690 I. 3D Printable Acrylate Polydimethylsiloxane Resins for Cell Culture and Drug Testing *Biomater. Sci.*  
691 2023, 11, 2950-2959.
- 692 (27) Zanon, M.; Montalvillo-Jiménez, L.; Cue-López, R.; Martínez-Campos, E.; Sangermano, M.;  
693 Chiappone, A.; Bosch, P. Vat 3D Printing of Full-Alginate Hydrogels via Thiol-Ene Reactions towards  
694 Tissue Engineering Applications *Polym. Chem.* 2023, 14, 4856-4868.
- 695 (28) Gugulothu, S.B.; Chatterjee, K. Visible Light-Based 4D-Bioprinted Tissue Scaffold *ACS Macro*  
696 *Lett.* 2023, 12, 494-502.
- 697 (29) Mo, X.; Ouyang, L.; Xiong, Z.; Zhang, T. Advances in Digital Light Processing of Hydrogels  
698 *Biomed. Mater.* 2022, 17, 042002.
- 699 (30) Cafiso, D.; Septevani, A.A.; Noè, C.; Schiller, T.; Pirri, C.F.; Roppolo, I.; Chiappone, A. 3D  
700 Printing of Fully Cellulose-Based Hydrogels by Digital Light Processing *SM&T* 2022, 32, E00444.
- 701 (31) Daly, A.C.; Critchley, S.E.; Rencsok, E.M.; Kelly, D.J. A Comparison of Different Bioinks for 3D

702 Bioprinting of Fibrocartilage and Hyaline Cartilage Biofabrication 2016, 8, 045002.  
703 (32) Li, S.; Huang, C.; Liu, H.; Han, X.; Wang, Z.; Huang, J.; Yan, Y.; Wang, Z. A Silk Fibroin  
704 Methacryloyl-Modified Hydrogel Promoting Cell Adhesion for Customized 3D Cell-Laden Structures  
705 ACS. Appl. Polym. Mater. 2022, 4, 7014-7024.  
706 (33) Villata, S.; Canta, M.; Baruffaldi, D.; Roppolo, I.; Pirri, C.F.; Frascella, F. 3D Bioprinted Gelma  
707 Platform for the Production of Lung Tumor Spheroids; Bioprinting 2023, 36, E00310.  
708 (34) Jing, X.; Xu, C.; Su, W.; Ding, Q.; Ye, B.; Su, Y.; Yu, K.; Zeng, L.; Yang, X.; Qu, Y. Photosensitive  
709 and Conductive Hydrogel Induced Innerved Bone Regeneration for Infected Bone Defect Repair Adv.  
710 Healthc. Mater. 2023, 12, 2201349.  
711 (35) Song, P.; Li, M.; Zhang, B.; Gui, X.; Han, Y.; Wang, L.; Zhou, W.; Guo, L.; Zhang, Z.; Li, Z. DLP  
712 Fabricating of Precision Gelma/HAP Porous Composite Scaffold for Bone Tissue Engineering  
713 Application Compos. B. Eng. 2022, 244, 110163.  
714 (36) Li, W.; Hu, X.; Liu, H.; Tian, J.; Li, L.; Luo, B.; Zhou, C.; Lu, L. 3D Light-Curing Printing to  
715 Construct Versatile Octopus-Bionic Patches J. Mater. Chem. B 2023, 11, 5010-5020.  
716 (37) Shen, J.; Song, W.; Liu, J.; Peng, X.; Tan, Z.; Xu, Y.; Liu, S.; Ren, L. 3D Bioprinting by  
717 Reinforced Bioink Based on Photocurable Interpenetrating Networks for Cartilage Tissue Engineering;  
718 International J. Biol. Macromol. 2024, 254, 127671.  
719 (38) Han, D.L.; Han, Y.J.; Li, J.; Liu, X.M.; Yeung, K.W.K.; Zheng, Y.F.; Cui, Z.D.; Yang, X.J.; Liang,  
720 Y.Q.; Li, Z.Y.; Zhu, S.L.; Yuan, X.B.; Feng, X.B.; Yang, C.; Wu, S.L. Enhanced Photocatalytic Activity  
721 and Photothermal Effects of Cu-Doped Metal-Organic Frameworks for Rapid Treatment of Bacteria-  
722 Infected Wounds Appl. Catal. B-Environ. 2020, 261, 118248.  
723 (39) Cao, Y.; Zhang, S.; Lv, Z.; Yin, N.; Zhang, H.; Song, P.; Zhang, T.; Chen, Y.; Xu, H.; Wang, Y. An  
724 Intelligent Nanoplatform for Orthotopic Glioblastoma Therapy by Nonferrous Ferroptosis Adv. Funct.  
725 Mater. 2022, 32, 2209227.  
726 (40) Zhu, Z.; Wang, L.; Peng, Y.; Chu, X.; Zhou, L.; Jin, Y.; Guo, H.; Gao, Q.; Yang, J.; Wang, X.  
727 Continuous Self-Oxygenated Double-Layered Hydrogel under Natural Light for Real-Time Infection  
728 Monitoring; Enhanced Photodynamic Therapy, and Hypoxia Relief in Refractory Diabetic Wounds  
729 Healing Adv. Funct. Mater. 2022, 32, 2201875.  
730 (41) Gastaldi, M.; Cardano, F.; Zanetti, M.; Viscardi, G.; Barolo, C.; Bordiga, S.; Magdassi, S.; Fin, A.;  
731 Roppolo, I. Functional Dyes in Polymeric 3D Printing: Applications and Perspectives ACS Materials  
732 Lett. 2020, 3, 1-17.  
733 (42) Jain, T.; Baker, H.B.; Gipsov, A.; Fisher, J.P.; Joy, A.; Kaplan, D.S.; Isayeva, I. Impact of Cell  
734 Density on the Bioprinting of Gelatin Methacrylate (Gelma) Bioinks Bioprinting 2021, 22, E00131.  
735 (43) Schuurman, W.; Levett, P.A.; Pot, M.W.; Van Weeren, P.R.; Dhert, W.J.; Hutmacher, D.W.;  
736 Melchels, F.P.; Klein, T.J.; Malda, J. Gelatin-Methacrylamide Hydrogels as Potential Biomaterials for  
737 Fabrication of Tissue-Engineered Cartilage Constructs Macromol. Biosci. 2013, 13, 551-561.  
738 (44) Shirahama, H.; Lee, B.H.; Tan, L.P.; Cho, N.-J. Precise Tuning of Facile One-Pot Gelatin  
739 Methacryloyl (Gelma) Synthesis Sci. Rep. 2016, 6, 31036.  
740 (45) Dai, W.; Zhang, L.; Yu, Y.; Yan, W.; Zhao, F.; Fan, Y.; Cao, C.; Cai, Q.; Hu, X.; Ao, Y. 3D  
741 Bioprinting of Heterogeneous Constructs Providing Tissue-Specific Microenvironment Based on Host-  
742 Guest Modulated Dynamic Hydrogel Bioink for Osteochondral Regeneration Adv. Funct. Mater. 2022,  
743 32, 2200710.  
744 (46) Zhu, T.; Jiang, C.; Wang, M.; Zhu, C.; Zhao, N.; Xu, J. Skin-Inspired Double-Hydrophobic-  
745 Coating Encapsulated Hydrogels with Enhanced Water Retention Capacity Adv. Funct. Mater. 2021, 31,

746 2102433.

747 (47) Sun, X.; Yang, J.; Ma, J.; Wang, T.; Zhao, X.; Zhu, D.; Jin, W.; Zhang, K.; Sun, X.; Shen, Y.;  
748 Three-Dimensional Bioprinted BMSCS-Laden Highly Adhesive Artificial Periosteum Containing  
749 Gelatin-Dopamine and Graphene Oxide Nanosheets Promoting Bone Defect Repair Biofabrication  
750 2023, 15, 025010.

751 (48) Aldana, A.A.; Valente, F.; Dilley, R.; Doyle, B. Development of 3D Bioprinted Gelma-Alginate  
752 Hydrogels with Tunable Mechanical Properties Bioprinting 2021, 21, E00105.

753 (49) Wang, Y.; Ying, M.L.; Zhang, M.; Ren, X.H.; Kim, I.S. Development of Antibacterial and  
754 Hemostatic PCL/Zein/Zno-Quaternary Ammonium Salts Nps Composite Mats as Wound Dressings  
755 Macromol. Mater. Eng. 2021, 306, 2100587.

756 (50) Nie, X.L.; Wu, S.L.; Mensah, A.; Wang, Q.Q.; Huang, F.L.; Li, D.W.; Wei, Q.F. Insight into Light-  
757 Driven Antibacterial Cotton Fabrics Decorated by In Situ Growth Strategy J. Colloid Interf. Sci. 2020,  
758 579, 233-242.

759 (51) Wang, Y.; Li, Z.; Liao, S.; Kong, Y.; Wang, Q.; Wei, Q. In Situ Biosynthetic BC/Zeolite Hybrid  
760 Hemostat for Quick Clot J. Appl. Polym. Sci. 2023, 140, E54315.

761 (52) Li, Y.; Chen, S.; Zhang, M.; Ma, X.; Zhao, J.; Ji, Y. Novel Injectable; Self-Healing; Long-Effective  
762 Bacteriostatic; and Healed-Promoting Hydrogel Wound Dressing and Controlled Drug Delivery  
763 Mechanisms ACS Appl. Mater. Interfaces 2024, 16, 2140-2153.

764 (53) Jin, P.X.; Wang, L.; Ma, X.L.; Lian, R.; Huang, J.W.; She, H.D.; Zhang, M.Y.; Wang, Q.Z.  
765 Construction of Hierarchical Zn<sub>2</sub>S<sub>4</sub>@PCN-224 Heterojunction for Boosting Photocatalytic  
766 Performance in Hydrogen Production and Degradation of Tetracycline Hydrochloride Appl. Catal. B-  
767 Environ. 2021, 284, 119762.

768 (54) Gastaldi, M.; Spiegel, C.A.; Vazquez-Martel, C.; Barolo, C.; Roppolo, I.; Blasco, E. 4D Printing of  
769 Light Activated Shape Memory Polymers with Organic Dyes Mol. Syst. Des. Eng. 2023,8, 323-329.

770 (55) Salas, A.; Pazniak, H.; Gonzalez-Julian, J.; Bianco, S.; Amici, J.; Ouisse, T.; Roppolo, I.; Cocuzza,  
771 M. Development of Polymeric/Mxenes Composites towards 3D Printable Electronics Compos. B. Eng.  
772 2023, 263, 110854.

773 (56) Ye, W.; Li, H.; Yu, K.; Xie, C.; Wang, P.; Zheng, Y.; Zhang, P.; Xiu, J.; Yang, Y.; Zhang, F. 3D  
774 Printing of Gelatin Methacrylate-Based Nerve Guidance Conduits with Multiple Channels Mater. Des.  
775 2020, 192, 108757.

776 (57) Shi, R.; Zhang, Z.; Yang, F.; Zhong, C. Simultaneously Anchoring Free Carboxyl and Sulfonate  
777 Groups into a Metal-Organic Framework for High Proton Conductivity Microporous Mesoporous  
778 Mater. 2022, 343, 112192.

779 (58) Xin, J.; Yang, Z.; Zhang, S.; Sun, L.; Wang, X.; Tang, Y.; Xiao, Y.; Huang, H.; Li, W. Fast  
780 Fabrication of "All-In-One" Injectable Hydrogels as Antibiotic Alternatives for Enhanced Bacterial  
781 Inhibition and Accelerating Wound Healing J. Nanobiotechnol. 2024, 221, 439.

782 (59) Janmaleki, M.; Liu, J.; Kamkar, M.; Azarmanesh, M.; Sundararaj, U.; Nezhad, A.S. Role of  
783 Temperature on Bio-Printability of Gelatin Methacryloyl Bioink in Two-Step Cross-Linking Strategy  
784 for Tissue Engineering Applications Biomed. Mater. 2020, 16, 015021.

785 (60) Wang, Y.; Ai, J.; Nie, X.; Li, Z.; Xia, X.; Hussain, T.; Wang, Q.; Wei, Q. Photodynamic Activity  
786 Enhanced by In Situ Biosynthetic BC/CQDs@PCN-224 Membranes through FRET Strategy;  
787 Carbohydr. Polym. 2023, 307, 120623.

788 (61) Turan, I.S.; Yildiz, D.; Turksoy, A.; Gunaydin, G.; Akkaya, E.U. A Bifunctional Photosensitizer for  
789 Enhanced Fractional Photodynamic Therapy: Singlet Oxygen Generation in the Presence and Absence

790 of Light Angew. Chem. Int. Ed. 2016, 55, 2875-2878.

791 (62) Zheng, X.; Zhong, J.; Dong, M.-Y.; Wen, Y.; Chen, A.-Z. Synthesis of Porphyrin-Based 2D  
792 Ytterbium Metal Organic Frameworks for Efficient Photodynamic Therapy; RSC Adv. 2022, 12,  
793 34318-34324.

794 (63) Lu, Z.; Gao, J.; Rao, S.; Jin, C.; Jiang, H.; Shen, J.; Yu, X.; Wang, W.; Wang, L.; Yang, J. A  
795 Multifunctional Membrane Based on TiO<sub>2</sub>/PCN-224 Heterojunction with Synergistic Photocatalytic-  
796 Photothermal Activity under Visible-Light Irradiation Appl. Catal. B-Environ. 2024, 342, 123374.

797 (64) Li, Z.; Liu, Z.; Ng, T.Y.; Sharma, P. The Effect of Water Content on the Elastic Modulus and  
798 Fracture Energy of Hydrogel Extreme Mech. Lett. 2020, 35, 100617.

799 (65) Mao, C.; Xiang, Y.; Liu, X.; Cui, Z.; Yang, X.; Yeung, K.W.K.; Pan, H.; Wang, X.; Chu, P.K.; Wu,  
800 S. Photo-Inspired Antibacterial Activity and Wound Healing Acceleration by Hydrogel Embedded with  
801 Ag/Ag@AgCl/ZnO Nanostructures ACS Nano 2017, 11, 9010-9021.

802 (66) Wang, B.; Xu, Y.; Shao, D.; Li, L.; Ma, Y.; Li, Y.; Zhu, J.; Shi, X.; Li, W. Inorganic Nanomaterials  
803 for Intelligent Photothermal Antibacterial Applications Front. Bioeng. Biotechnol. 2022, 10, 1047598.

804 (67) Wang, Y.; Nie, X.; Lv, Z.; Hao, Y.; Wang, Q.; Wei, Q. A Fast Hemostatic and Enhanced  
805 Photodynamic 2-Dimensional Metal-Organic Framework Loaded Aerogel Patch for Wound  
806 Management J. Colloid Interf. Sci. 2024, 656, 376-388.

807 (68) Li, Q.; Hu, E.; Yu, K.; Xie, R.; Lu, F.; Lu, B.; Bao, R.; Dai, F.; Lan, G. Gemini Dressing with both  
808 Super-Hydrophilicity and-Hydrophobicity Pursuing Isolation of Blood Cells for Hemostasis and  
809 Wound Healing Adv. Fiber Mater. 2023, 5, 1-20.

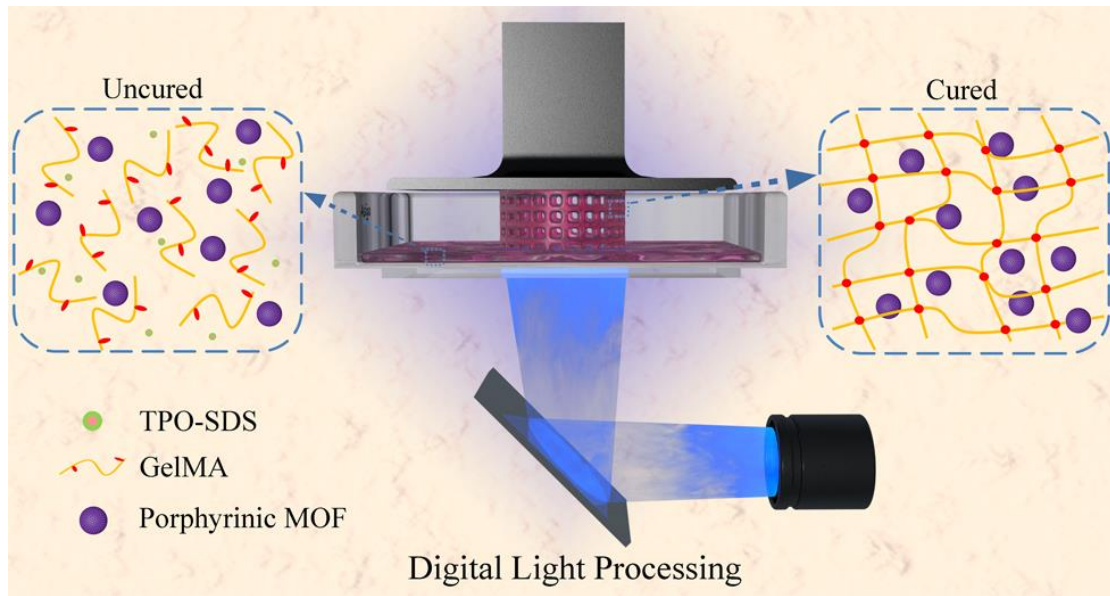
810 (69) Peng, X.; Xu, X.; Deng, Y.; Xie, X.; Xu, L.; Xu, X.; Yuan, W.; Yang, B.; Yang, X.; Xia, X.  
811 Ultrafast Self-Gelling and Wet Adhesive Powder for Acute Hemostasis and Wound Healing Adv. Funct.  
812 Mater. 2021, 31, 2102583.

813 (70) Long, M.; Zhang, Y.; Huang, P.; Chang, S.; Hu, Y.; Yang, Q.; Mao, L.; Yang, H. Emerging  
814 Nanoclay Composite for Effective Hemostasis Adv. Funct. Mater. 2018, 28, 1704452.

815

816  
817  
818

### Table Of Contents (TOC)



819  
820